Size dependent response of large shell elements under in-plane tensile loading

CrossMark

M. Kõrgesaar *, H. Remes, J. Romanoff

Aalto University, School of Engineering, Department of Applied Mechanics, P.O. Box 12200, FIN-00076 Aalto, Finland

ABSTRACT

Large-scale thin-walled structures with a low weight-to-stiffness ratio provide the means for cost and energy efficiency in structural design. However, the design of such structures for crash and impact resistance requires reliable FE simulations. Large shell elements are used in those simulations. Simulations require the knowledge of the true stress–strain response of the material until fracture initiation. Because of the size effects, local material relation determined with experiments is not applicable to large shell elements. Therefore, a numerical method is outlined to determine the effect of element size on the macroscopic response of large structural shell elements until fracture initiation. Macroscopic response is determined by introducing averaging unit into the numerical model over which volume averaged equivalent stress and plastic strain are evaluated. Three different stress states are considered in this investigation: uniaxial, plane strain and equi-biaxial tension. The results demonstrate that fracture strain is highly sensitive to size effects in uniaxial tension whereas in plane strain or equi-biaxial tension size effects are much weaker. In uniaxial and plane strain tension the fracture strain for large shell elements approaches the Swift diffuse necking condition.

© 2014 Elsevier Ltd. All rights reserved.

1. Introduction

Thin-walled structures with a low weight-to-stiffness ratio provide the means for cost- and energy efficiency in structural design. In the quest for efficiency, the structural safety of lightweight shell structures has become more important as a result of the increased societal awareness regarding accidents and structural failure. This has led to designs that rely on FE simulations as full-scale experiments of such events are impossible to conduct. Simulations involving impact, crush and crashworthiness however, require the knowledge of true stress–strain behavior of the material until fracture initiation.

Recent experimental–numerical studies, e.g. (Zhang et al., 1999; Gruben et al., 2012; Dunand and Mohr, 2010; Tardif and Kyriakides, 2012; Ghahremaninezhad and Ravi-Chandar, 2012), clearly show that an accurate stress–strain response and equivalent plastic strain to fracture initiation $\bar{\varepsilon}^f$, i.e. the fracture strain, are a pre-condition for adequate FE solution in problems involving strain localization and ductile fracture. For the sake of brevity, notation "fracture strain" is used throughout the paper interchangeably with the term "fracture initiation strain". In these studies the stress–strain relation and the fracture strain are determined using a certain experimental length scale. This experimental length scale defines the element size used in the simulations; see e.g. (Hogström et al., 2009; Ehlers and Varsta, 2009). In other words, the FE solution is mesh size sensitive, which accuracy depends on the chosen fracture strain. In the failure analysis of materials and structures, such size effects are an important issue (Bazant, 2000; Fleck and Hutchinson, 1993). In large-scale structural analysis, for practical reasons, the mesh size is usually several orders of magnitude higher than the experimental length scale. For instance, the recommended element aspect ratio in the analysis of large structures is $L_e/t > 5$, where L_e is the element length and t is the plate thickness (Hogström and Ringsberg, 2012). In contrast, the aspect ratio corresponding to the experimental length scale is usually less than 1. Hence, the consistency between the experimental length scale and FE mesh size is lost.

The engineering approach to bridging the two scales is the most intuitive. By introduction of "virtual extensometer", which represents various experimental length scales in a standard tensile test, fracture strain can be determined for larger elements. Stress on the other hand cannot be directly measured, which is why it is calculated based on the minimum cross-sectional area of the specimen independent of the experimental length scale. The true stress–strain curve until fracture obtained this way represents the macroscopic response of large structural shell elements until fracture initiation. Alternatively, for the one-dimensional uniaxial tension case, a

* Corresponding author. Tel.: +358 50 5648878; fax: +358 947024173.
E-mail address: mihkel.korgesaar@aalto.fi (M. Kõrgesaar).

closed-form analytical expression of the element size to the fracture strain can be derived (Li and Karr, 2009). In any case, the power-law type relationship that relates fracture strain to element size is denoted as Barba's law. Fracture criterion that is based on the critical equivalent plastic strain and is scaled with the Barba's law is referred to as *shear* criterion. This fracture criterion is employed most notably in the analysis of large-scale structural components (Simonsen and Törnqvist, 2004; Alsos et al., 2009; Hogström and Ringsberg, 2013; Ehlers, 2010) and full-size collision and crashworthiness simulations of ship structures, e.g. (Naar et al., 2002; Yamada et al., 2005; Kõrgesaar and Ehlers, 2010; Samuelides, 2012; Hogström and Ringsberg, 2012) to name a few. However, the *shear* criterion is strictly valid only for uniaxial tension. It is known that the fracture ductility is a strong function of the stress state or the stress triaxiality, $\eta = \sigma_h/\bar{\sigma}$, where the hydrostatic and von Mises stress are denoted by σ_h and $\bar{\sigma}$, respectively. Stress state-dependent failure in metals was first observed by McClintock (1968), Rice and Tracey (1969), Hancock and Mackenzie (1976), Gurson (1977) and Johnson and Cook (1985) and in more recent experimental studies, e.g. (Bao and Wierzbicki, 2004; Barsoum and Faleskog, 2007; Haltom et al., 2013; Hopperstad et al., 2003). An example of the influence of triaxiality on the fracture strain in plane stress condition is shown for a steel material in Fig. 1(a). The results of the tensile experiments by Dunand and Mohr (2010) with different notch radii in Fig. 1(b) clearly indicate that the fracture strain is also strongly dependent on the strain path. The importance of stress triaxiality on the fracture strain is also recognized by some of the fracture criteria employed in large-scale structural analysis, namely the Bressan–Williams–Hill (BWH) instability and the Rice–Tracey–Cockcroft–Latham (RTCL) damage criterion described by Alsos et al. (2008) and Törnqvist (2003), respectively. However, the BWH-criterion neglects the size effects completely, as it is argued that size effects appear after local necking. The RTCL criterion is adjusted for different mesh densities based on the fracture strain determined with the uniaxial tension test, i.e., with a Barba's law. Walters (2013) has proposed adjusting the fracture strain on both the mesh size and stress state. However, evidence for such an adjustment is still lacking as no experimental or numerical results were presented.

To fill this gap, we introduce an alternative numerical approach to bridge the local and global scale and thereby describe the size effects at different stress states. The numerical stress–strain response until fracture in global scale, referred to as macroscopic response, is obtained as the volume averaged stress–strain response of a finite averaging unit (AU) that is introduced into the numerical model or specimen. The specimen is imposed to stress states corresponding to multi-axial tension condition: uniaxial tension (UAT, $\eta = 1/3$), plane strain tension (PST $\eta = 1/\sqrt{3}$)

and equi-biaxial tension (EBT, $\eta = 2/\sqrt{3}$). Size effects due to the bending are not considered in the present study. Thereby, the combined effect of size and stress state on the fracture strain is established. Size of the averaging unit corresponds to the large structural shell elements used in the analysis of large structures such as ships. Hence, the approach described is fundamentally an extension of the engineering approach used to determine Barba's law from tensile tests to multi-axial stress states. In contrast to engineering approach described above, "averaging unit" introduced to numerical model facilitates the comprehensive analysis of all the field quantities, including the stress and strain state, and their influence on the true stress–strain response and the fracture strain.

2. Approach

2.1. Necking instability

In general, a ductile fracture in sheet metal is preceded by a loss of stability, (Marciniak and Kuczyński, 1967; Hutchinson and Neale, 1979; Xue, 2010). The loss of stability reveals itself during the deformation process as high strain and stress gradients appear over a limited region of the sheet, while in the exterior zones some unloading and softening can take place. This type of plastic flow localization is responsible for the size effects investigated in this study. Depending on the stress state, the intensity of the plastic flow and the size of the localization zone vary. Thereby, the intensity of the size effects in different stress states can vary as well. Specifically, we consider two types of instabilities: diffuse and localized necking. Diffuse necking, which is characteristic of flat tensile specimens and uniaxial tension ($\eta = 1/3$), takes place over the width of the gage section as shown in Fig. 2(a). The amount of diffuse necking is here quantified as the width ratio at the end of the gage section (w_1) vs. the width in the middle section (w_2). Diffuse necking is followed by localized necking, or severe thinning in the middle of the gage section. In metals the width of the local neck is roughly equal to the thickness of the sheet (Hu et al., 2002). The amount of thinning is quantified with the thickness ratio of t_1/t_2 as shown in Fig. 2(a)–(c). This ratio starts to increase already in the diffuse necking stage, but the localized necking triggers a steep growth of the ratio. Therefore, the thickness ratio is associated with the developing local neck. In plane strain ($\eta = 1/\sqrt{3}$) and equi-biaxial tension ($\eta = 2/3$), geometric constraints obviate the diffuse necking, meaning that only localized necks appear in the thickness direction. Geometric constraint in plane strain stems from the boundary conditions, which restrict the plate edges from pulling in as shown in Fig. 2(b), and in equi-biaxial tension from the loading as shown in Fig. 2(c), which
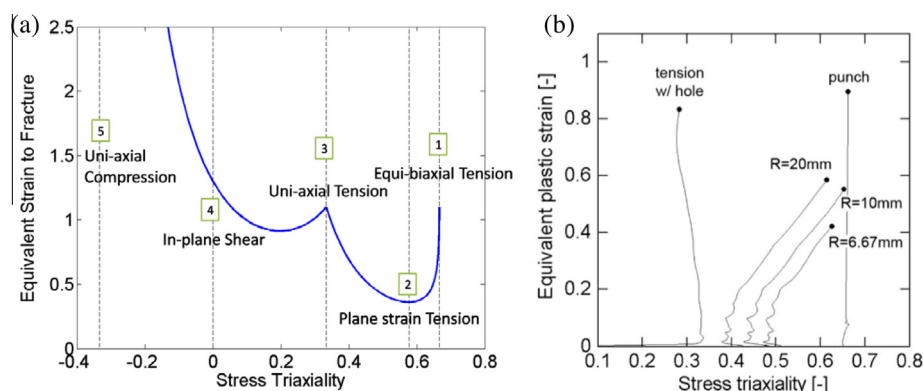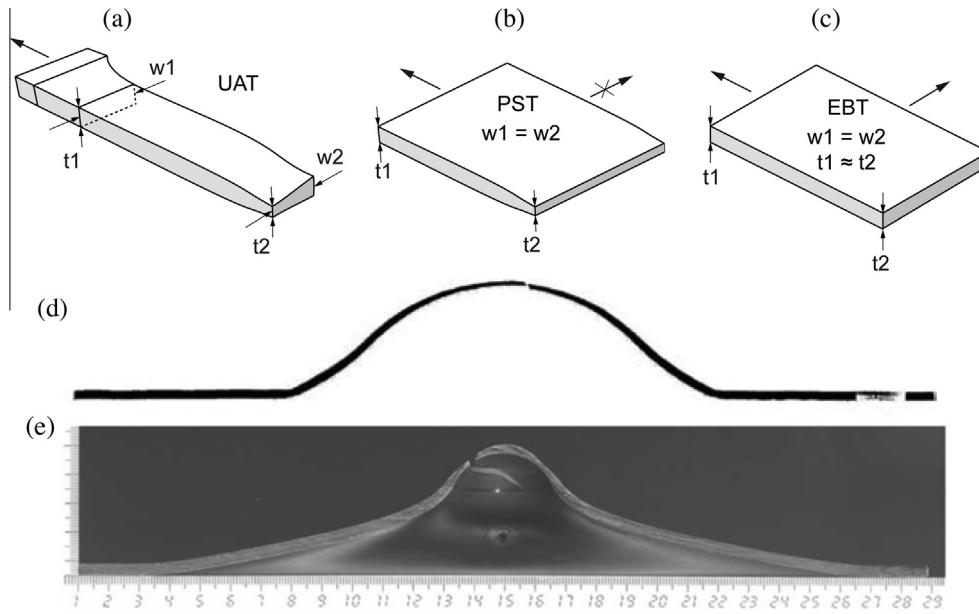

Fig. 1. Influence of stress triaxiality on fracture ductility for two advanced high-strength steels. (a) Fracture envelope from Luo and Wierzbicki (2010) and (b) triaxiality history until fracture initiation for three different specimens (Dunand and Mohr, 2010).

Fig. 2. Necking in metal sheets. Quarter of the (a) tensile, (b) plane strain and (c) equi-biaxial tension specimen. UAT specimen displays diffuse and local neck, while PST specimen shows only local neck. In EBT thinning is almost uniform. (d) and (e) show the cut of the fractured specimen stretched over a punch in the biaxial strain path. Extensive thinning of the specimen is evident and the local neck is barely noticeable. Figure (d) is for aluminum (Beese et al., 2010) and (e) is for normal-strength steel (Ehlers, 2010).

does not provide any preference in direction for the neck development. In equi-biaxial tension the geometric constraint is strong enough to prevent a localized neck from reaching the plane strain path, which is necessary for the neck to grow (Tasan et al., 2009). This will result in excessive thinning of the specimen prior to localization as shown in Fig. 2(d) and (e) that leads to a very high fracture strain – the fracture strain in equi-biaxial tension is comparable to the fracture strain in uniaxial tension as shown in Fig. 1.

2.2. Averaging procedure

Because of the necking, the volume averaged equivalent stress and plastic strain are subject to size effects. To determine this effect an "averaging unit" (AU) is introduced into the numerical FE model. The averaging unit is built up from small elements with a size of $L_e/t < 0.2$; in this investigation both solid and shells are used. The response of these small elements is characterized with the true stress–strain curve and fracture strain, which can be obtained experimentally, e.g. see Ehlers and Varsta (2009). The size of the averaging unit is equal to the FE size commonly used in the analysis of large-scale structural components. Therefore, the local response averaged over the averaging unit is denoted as the macroscopic response. Point of fracture initiation in the averaging unit corresponds to the failure of the first material point, represented by a single shell or solid element. Averaging unit is loaded such that the macroscopic stress triaxiality remains nearly constant throughout the entire loading history and corresponds to uniaxial tension (UAT), plane strain tension (PST) or equi-biaxial tension (EBT). Only the plastic strain components are inspected in the averaging unit, as the elastic strains are negligible in metals with extensive plastic region. The macroscopic behavior of the averaging unit at time instant i is characterized with the volume averaged equivalent stress $\bar{\sigma}_V^i$, equivalent plastic strain $\bar{\varepsilon}_V^i$ and stress triaxiality η_V^i evaluated throughout the deformation process:

$$\bar{\sigma}_V^i = \frac{\int_V \bar{\sigma}^i dV^i}{\int_V dV^i};$$ (1a)

$$\bar{\varepsilon}_V^i = \frac{\int_V \bar{\varepsilon}^i dV^i}{\int_V dV^i};$$ (1b)

$$\eta_V^i = \frac{\int_V \eta^i dV^i}{\int_V dV^i},$$ (1c)

where $\bar{\sigma}^i$, $\bar{\varepsilon}^i$ and η^i are the equivalent stress, equivalent plastic strain and stress triaxiality of a single small element at time instant i, respectively; dV is the volume of an element and V is the total volume of the averaging unit. In order to construct the fracture locus in the $\bar{\varepsilon}_f - \eta$ space, time averaged stress triaxiality η_a at the point of fracture initiation is introduced, defined by

$$\eta_a = \frac{1}{\bar{\varepsilon}_f} \int_0^{\bar{\varepsilon}_f} \eta d\bar{\varepsilon}.$$ (2)

2.3. Finite element modeling

Three different types of geometries were used, see Fig. 3. Desired macroscopic stress state in the AU is achieved by setting the proper boundary conditions. Thickness of the specimens is t and the rest of the dimensions are chosen in order to accommodate the two AUs. The size of the AU is normalized with respect to the thickness of the sheet: L_e/t. Therefore, in the sequel L_e/t ratio is appended to the AU term to distinguish between the two chosen AU sizes. In Fig. 3 AU10 does not only surround AU6, but also encompasses it. Two FE models were created for each specimen in order to study the influence of the plane stress assumption of shell elements on the macroscopic behavior: one with solid and the other with shell elements. The elements utilize reduced integration and thus the solid and shell elements have eight and four nodes respectively (C3D8R, S4R in ABAQUS); the shell elements have five integration points through their thickness.

2.3.1. Solid model

Only 1/8th of the UAT and PST specimens were modeled, as shown in Fig. 3(a) and (b), provided by the symmetry of both
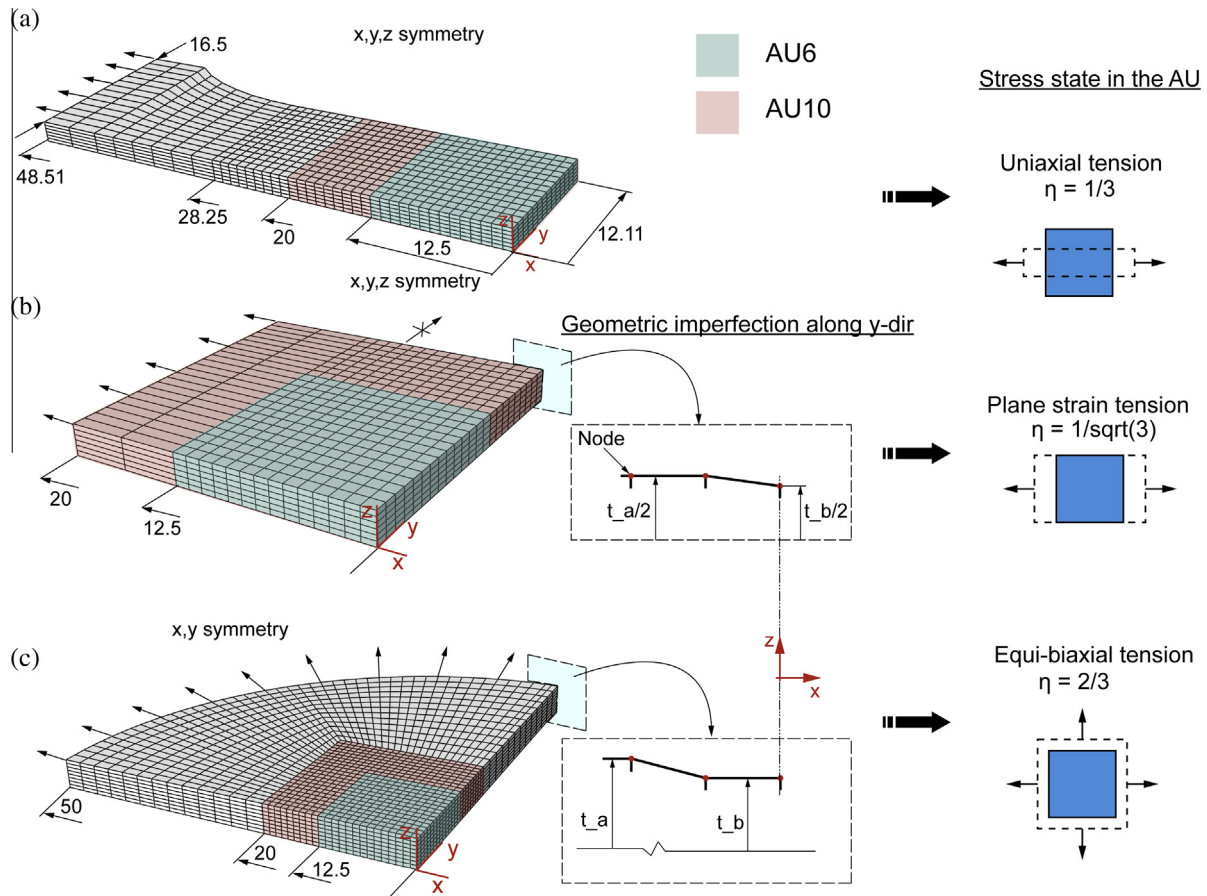
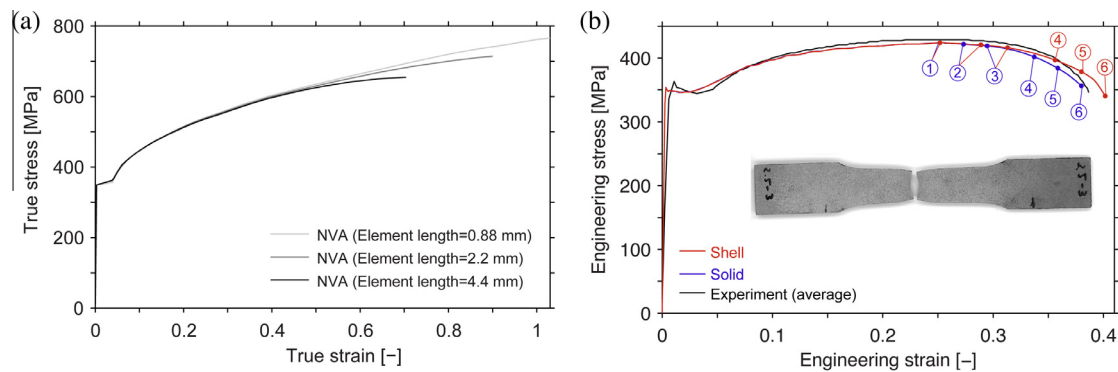**Fig. 3.** Finite element models. (a) UAT, (b) PST, and (c) EBT specimen.

Fig. 4. (a) Element length-dependent true stress–strain relation – data from Ehlers and Varsta (2009). (b) Measured and simulated engineering stress–strain response results for the UAT.

specimens in all three directions. It must be pointed out however that localized necking in uniaxial tension occurs along a line inclined to the normal of the tensile direction. Often bifurcation into a mode occurs, in which only one of the two localized necks continue to develop (Tvergaard, 1993). This however is not allowed by the assumed symmetries. Nevertheless, one case study with the full solid model showed that two localized necks grow simultaneously and localization in current specimen is symmetric, as is the experimental fracture path that is shown in Fig. 4(b). Therefore, the assumed symmetries are justified. In the PST specimen a small geometric imperfection, i.e., a Marciniak defect (Marciniak and Kuczyński, 1967), was introduced across the width of the sheet (y-direction), as shown in Fig. 3(b), to trigger the localization in the middle of the specimen. Without the imperfection the

deformation localized to the edge where the displacement was applied. This initial inhomogeneity is described with the thickness ratio $f = t_b/t_a = 0.99$, where t_a is the thickness of the sheet outside of the groove, while that in the groove is t_b. In the EBT specimen symmetry was employed only in x- and y-direction because of the two coordinate systems employed – cylindrical coordinate system was used to apply velocity on the boundary while rectangular Cartesian coordinate system was used to apply symmetry, see Appendix A for details. Similar defect as in the PST specimen was implemented to obtain a necking instability in the calculation. Without the defect, in the classical J2 flow theory, the localization is predicted never to occur under equi-biaxial strain paths (Hutchinson and Neale, 1979; Dequiedt, 2011). The severity of the defect in the EBT specimen is $f = 0.98$. In the UAT specimen no imperfection

was introduced as the localization occurred in the middle of the specimen without a defect. In the UAT and PST models, there are six elements through the half-thickness, while in the EBT model with full thickness there are eight elements through the thickness. The number of through-thickness elements is defined on the basis of the convergence analysis carried out only with the tensile test. Mesh refinement showed that engineering stress did not change more than 1%. Tensile test was chosen since this is the most critical case in terms of through thickness stress and strain gradients.

2.3.2. Shell model

In the shell element models the in-plane element topology is the same as in the solid models. In all cases, the symmetry was again exploited by modeling only a quarter of the specimen. The imperfections in the PST and EBT models were implemented at the same location as in the solid models by means of an equivalent thickness reduction. The imperfect zone is restricted to one element width.

2.3.3. Simulations

Numerical simulations were carried out with the commercial code ABAQUS/Explicit v6.11-2 (ABAQUS, 2011). All the simulations were displacement controlled. The simulations were stopped once the first element was deleted. The total step time was chosen to be long enough to ensure a quasi-static analysis of the simulations, i.e., the ratio of the kinematic energy to the total energy is less than 5%.

3. Results

3.1. Material and constitutive modeling

The data used in the analysis is obtained from Norske Veritas grade A (NVA) RAEX S275 laser steel by Ruukki; see Fig. 4(a). The grade A material is commonly used in shipbuilding, where large shell elements are often employed in FE modeling. The material was tensile tested by Ehlers and Varsta (2009) using an optical strain measurement system. This data is used in the numerical analysis; for the numeric values see Table B1 in Appendix. The geometry of our FE model in Fig. 3(a) corresponds to tensile specimen tested by Ehlers and Varsta with the length-to-breadth ratio of 8 with gauge length of 56.5 mm; the plate thickness t is 4.04 mm. The Young's modulus is 206 GPa, the Poisson's ratio is 0.3 and the measured yield stress is 349 MPa. For 0.88-mm element length the measured fracture strain in uniaxial case is $\bar{\varepsilon}_f = 1.018$. We emphasize that this value is measured in the surface of the specimen, and as such it is not representative for the strain to fracture in the middle of the material (Dunand and Mohr, 2010). Nevertheless, the accuracy is sufficient for the purpose of this paper wherein volume averaged strains and stresses are calculated. The selection of fracture strain for plane strain and equi-biaxial tension is based on Fig. 1. Thus, in EBT the fracture strain is taken equal to that of uniaxial tension, i.e. $\bar{\varepsilon}_f = 1.018$. In PST, half of this is utilized, i.e. $\bar{\varepsilon}_f \cong 0.51$.

The measured and simulated engineering stress–strain responses of the UAT specimen are compared in Fig. 4(b). Good correspondence is obtained with the solid model, especially at high engineering strains, while the shell model overestimates the deformations by a few percent. Subsequently, the deformations at the marked points in the descending part of Fig. 4(b) will be analyzed.

3.2. Equivalent stress and plastic strain

3.2.1. Specimen

In Fig. 5(a)–(d) the equivalent stress and plastic strain are plotted for the UAT specimen at the stages 1–6. The similar curves for the PST are plotted in Fig. 5(e) and (f) and for the EBT in (g) and

(h). The curves correspond to the dimensionless displacement δ/δ_f, where δ is the change in the displacement and δ_f is the displacement to fracture initiation. These profiles are extracted along a path in the middle (mid-width and mid-thickness) of the specimen.

In the UAT the strain curves ($\bar{\varepsilon}$) between the shell in Fig. 5(a) and the solid model in Fig. 5(c) are very similar. At the maximum load, point ①, the deformation is still uniform in both models. With increasing deformation a breadthwise diffuse neck builds up, which gradually grows into a localized neck in thickness direction. From point ④ onwards, the localization is very distinct but the specimen has still some capacity to deform in the thickness direction. Outside the necked region the strain remains unchanged. The equivalent stress in Fig. 5(b) and (d), on the other hand, contrast more, especially in the necking stage. At point ④, unloading and softening of the models outside of the necked region is clearly visible. The unloading process continues outside of the neck until the final stage of ⑥, when the stress in the shell model localizes into the smallest possible area allowed by the mesh, i.e., a single row of elements across the width. The solid model distributes the stress more evenly over the entire specimen as expected.

In PST the solid model results in Fig. 5(e) show that fracture strain in the middle of the neck is approximately twice as high as the uniform strain outside of the neck. Because the shell model cannot redistribute thickness directional stress, the stresses and strains outside of the neck are lower than in the solid model. Fig. 5(f) indicates that stress softening in the solid model is weaker than in the UAT in Fig. 5(d). In general, the stress and strain behavior is different from the UAT results because only through-thickness neck prevails. The equivalent plastic strain curves for EBT in Fig. 5(g) indicate that the strain in the neck is only few percent higher than the strain in the rest of the model. In contrast to the UAT and PST, the strain outside of the localization zone increase throughout the deformation process – the sheet goes through excessive thinning, as described in Section 2.1. Consequently, the equivalent stress in Fig. 5(h) exhibits no softening, which was clearly present for the other analyzed stress states. The differences between the shell and solid results are similar to those in the PST case. Fig. 5 clearly shows that the localization is strongest in the UAT and weakest in the EBT. This can be explained by the high strain gradients in both the width and the longitudinal direction of the UAT specimen, as evidenced in Fig. 6. Since there is no diffuse neck present in the PST and EBT path, the strain gradient develops only in one direction, which in turn limits the intensity of the localization.

#### 3.2.2. Averaging unit (AU)

The equivalent stress plastic strain response of the AUs is evaluated according to Eqs. (1a) and (1b); see Fig. 7. The marked points ① and ⑥ identify the maximum load and point of fracture initiation as given in Fig. 4(b), respectively. The amount of diffuse necking (w_1/w_2) and thinning (t_1/t_2) are displayed on the second y-axis as the ratio, both taken from the solid model. Both ratios are plotted in Fig. 7 using an equivalent plastic strain corresponding to the AU6.

In UAT after the load maximum, the macroscopic response in both AUs is still of the hardening type. However, once the localized necking commences the curves start to deviate from the input hardening curve. Up to a certain point the rate of thinning coincides with the rate of width reduction, which is characteristic in diffuse necking. Beyond that point, the thinning of the model becomes considerably more pronounced, and the stress–strain response starts to deviate from the initial hardening curve. This suggests that the softening of the stress–strain curve is related to the localized necking in thickness direction rather than diffuse necking. Finally, the UAT curves are clearly sensitive to the size of the AU as the fracture strain decreases once the averaging volume increases.

In case of PST and EBT, the shell models tend to fail earlier. This is attributed to the localized necking in the thickness direction,
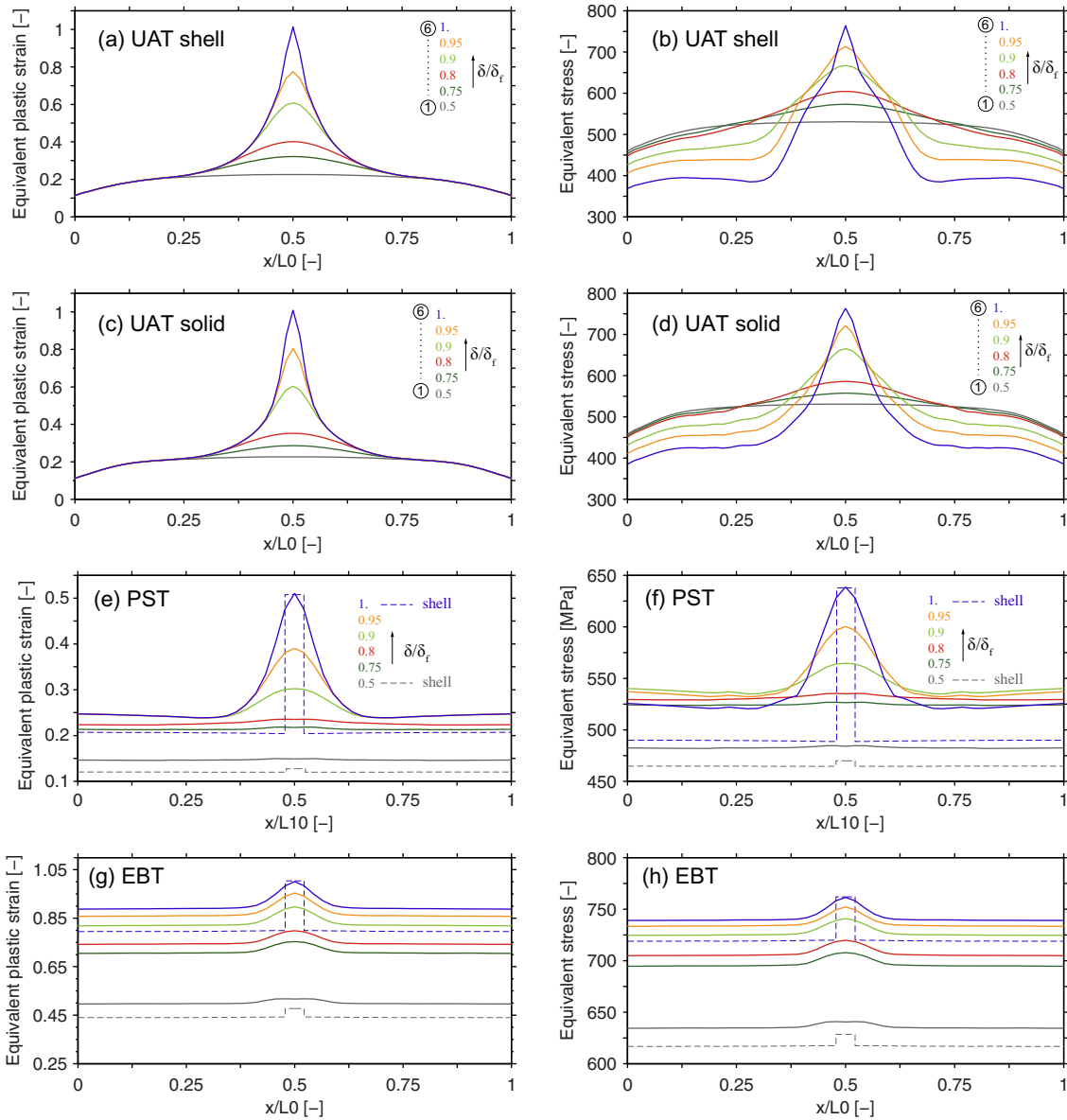
Fig. 5. Simulated equivalent plastic strain (left-hand column) and equivalent stress (right-hand column) along the centerline of the FE models. (a) and (b) UAT shell model; (c) and (d) UAT solid model; (e) and (f) PST; (g) and (h) EBT. x-axis is normalized with respect to the initial gage length of the specimen L_g = 28.25·2 = 56.5 mm in UAT, while in PST L_{10} = 40 mm.
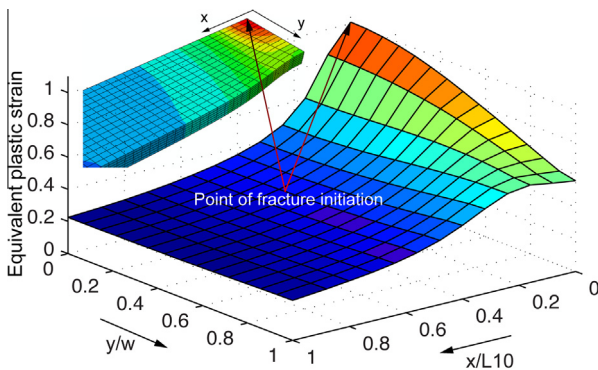
Fig. 6. Equivalent plastic strain localization in the UAT simulation.

which shell elements cannot reliably capture. Therefore, we concentrate on the solid model results. The amount of thinning is again quantified on the second y-axis as t_1/t_2, but now t_1

corresponds to the thickness taken from 20 mm away from the centerline; at the boundary of AU10. In contrast to the UAT results, the influence of the AU size on the fracture strain is barely noticeable. In plane strain, some size effects appear after the softening begins. The softening is again attributed to the localized necking quantified by the thickness ratio, which shows a sudden increase approximately at the start of the softening. In the EBT, the intensity of the thinning is negligible in the neck. This was also implied by the weak strain gradients in Fig. 5(g). Hence, there is no softening.

3.3. Stress state and the strain path to fracture initiation

First, it was confirmed that the averaging unit is in the plane stress condition by calculating the volume averaged through thickness stress. This justifies that the macroscopic response is applicable to large shell elements.

Fig. 8 summarizes the strain paths for all three cases in the space of stress triaxiality and the equivalent plastic strain. A
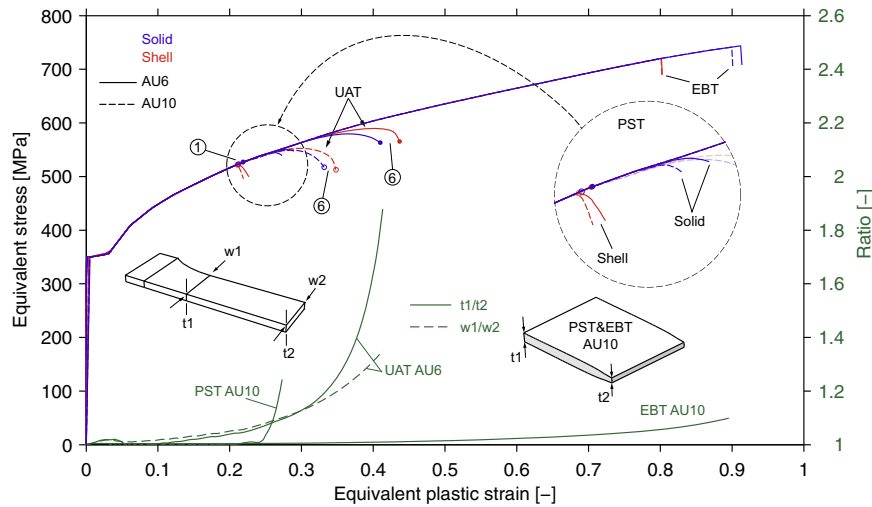
Fig. 7. Equivalent stress plastic strain response in the AUs and the amount of necking.

distinction is made between a single element in the middle of the model (mid-span, mid-width and mid-thickness), in which the highest strain develops, and the macroscopic response observed in the AUs; see Eq. (1c). Once again, the fact that the stress state becomes non-uniform at the maximum load in the UAT path, point ①, is evidenced by the bifurcating paths. Locally the stress state advances towards the plane strain state ($\eta = 1/\sqrt{3}$) whereas macroscopically plane strain does not prevail and the stress state advances towards the opposite, shear side. The developing thickness strain in the middle of the PST model also increases the stress triaxiality. In the EBT the stress state remains nearly constant throughout the process. The stress triaxialities at fracture initiation calculated with Eq. (2) are also shown in Fig. 8. They confirm that the time-averaged stress triaxiality in the AUs is characteristic in all cases and is in line with the aspired stress state: UAT ($\eta = 1/3$), PST ($\eta = 1/\sqrt{3}$) and EBT ($\eta = 2/3$).

3.4. Size effects

The results in Fig. 8 are visualized once again in Fig. 9 in order to be able to comprehend the influence of the AU size and stress state on the fracture strain. The time-averaged stress triaxiality at fracture initiation calculated with Eq. (2) is used in Fig. 9. Because of this the average stress triaxiality at fracture initiation in local scale does not exactly correspond to the pure UAT or PST, as it does for the macroscopic AUs. Fig. 9(a)–(c) contain the current results, but different analytical curves are fitted through the data in Figs. (b) and (c).
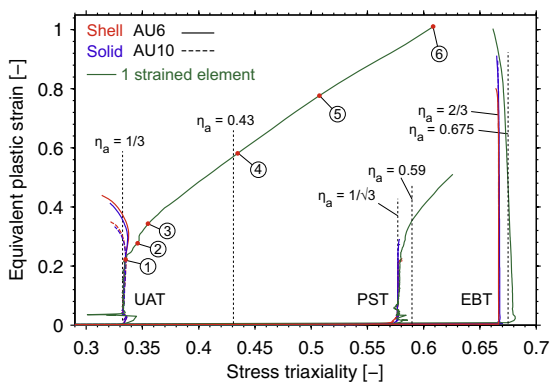

Fig. 8. Stress triaxiality and equivalent plastic strain history in the AUs and in the element that fails first.

Fig. 9(a) displays how the macroscopic fracture initiation strain varies depending on the stress state. Size effects are clearly dependent on the stress state imposed on the AU. In the UAT the decrease in the fracture strain is clearly more significant than in the PST and especially in the EBT. Moreover, while in the PST and EBT some size effects appear when moving from 0.88 mm elements ($L_e/t = 0.2$) to AU6, these effects disappear when moving from AU6 to AU10. In the UAT, the fracture strain is still decreasing.

In Fig. 9 (b) two fracture criteria commonly employed in large-scale simulations are plotted: the *shear* criterion and the RTCL criterion; description of the RTCL criterion is given in Appendix C. Both criteria are calibrated with the Barba's law. If the *shear* criterion is used for small elements the fracture energy is correctly predicted in the EBT and UAT, but not in the stress states between. However, for large elements (AU6 and 10) the error is significant only for the EBT. For EBT the RTCL criterion gives similar error in large elements. On the other hand, in small elements RTCL criterion predicts fracture strain more realistically between the UAT and PST than the *shear* criterion.

In Fig. 9(c) the fracture criterion of Lou et al. (2012) is fitted through the input fracture data we used in the analyses; criterion given in Appendix C. Furthermore, because of the notion that the results should be size-independent before necking, we also plotted two instability criteria in Fig. 9(c): Swift diffuse and the BWH localized necking criterion (Appendix C). Curves are plotted for a strain-hardening material $\bar{\sigma} = K\bar{\varepsilon}^n$, where $K = 750$ and $n = 0.24$, fitted on the basis of the true stress–strain response in Fig. 4(a). Fig. 9(c) shows that the UAT results approach the analytical Swift diffuse necking condition and the PST results lie exactly on the curve, i.e., the fracture strain becomes size-insensitive at this point, as it should. However, in the EBT the size insensitivity appears much earlier than predicted by the Swift criterion.

As the BWH criterion is argued to be suitable for very large elements (Alsos et al., 2008), we compare this criterion with the AU10 data. In the UAT the criterion overestimates the fracture strain, while in the EBT it underestimates the strain. Nevertheless, in the EBT the criterion gives a better estimate than the diffuse necking condition.

4. Discussion

4.1. Size effects and necking

The size effects are a consequence of the two necking modes observed here. In the UAT the size effects manifest themselves
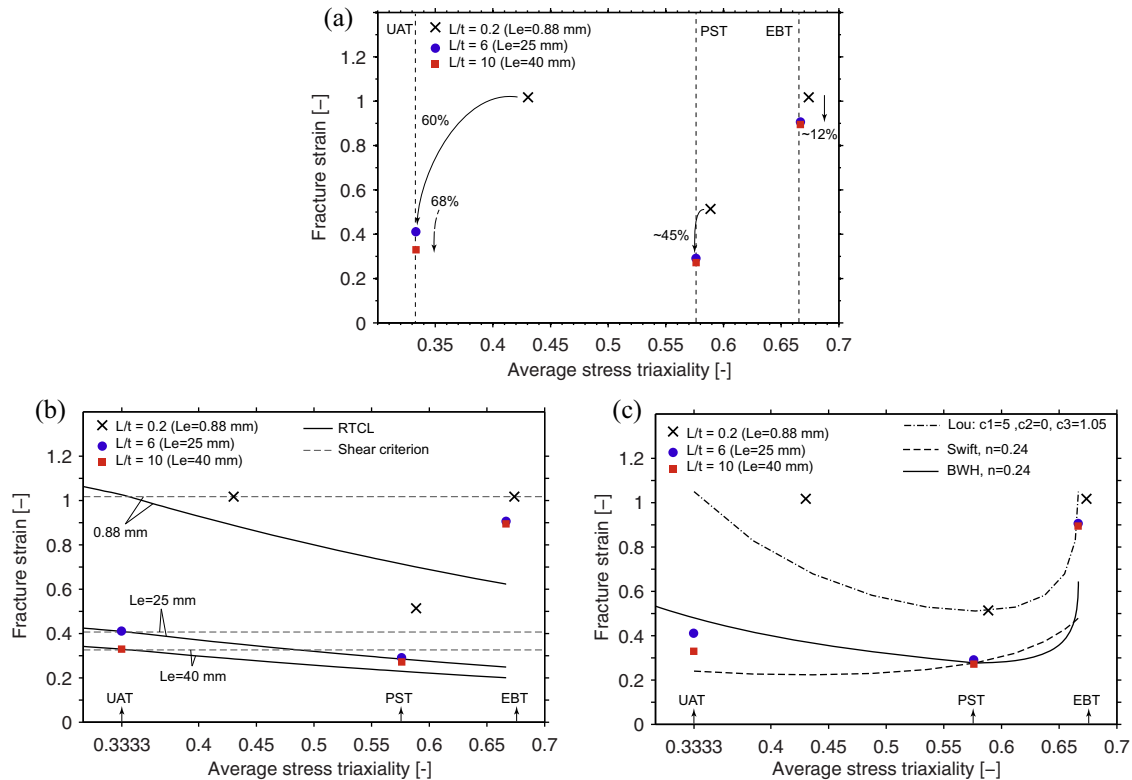
Fig. 9. Size effects at different stress states. (a) Current results. Results compared with (b) mesh size dependent fracture criteria and (c) analytical instability criteria.

through a combination of diffuse and localized necking, resulting in high strain gradients in both the width and the longitudinal direction, as evidenced in Fig. 6. In the PST and EBT path, only local neck appears. This limits the intensity of the localization and delivers less sensitive fracture strain in Fig. 9. A comparison of the fracture criterion applicable on a small scale (Lou et al., 2012) and the Swift condition providing the lowest bound to the fracture data indicates that the shape of the initial fracture envelope is not retained as a result of the size effects. The difference in this change of shape is particularly noteworthy between the UAT and PST: the difference in the fracture strain in small elements is ∼50%, while in large elements this difference is reduced to only a few percent. The relatively weak size effects observed in the EBT additionally contribute to this change of shape. This observation explains the relative success of the RTCL and especially the *shear* criterion in the ship collision and grounding simulations, in which the large shell elements are used (Simonsen and Törnqvist, 2004; Naar et al., 2002; Hogström and Ringsberg, 2013; Ehlers et al., 2008). At the same time, the large discrepancy in the EBT might explain the relative ineffectiveness of the criteria to capture the experimental results in cases where failure occurs predominantly in stress states between the plane strain and equibiaxial tension. This point is well exhibited by the numerical simulations of Alsos et al. (2009), who employed the RTCL criterion to simulate plate impact with the rigid indenter.

Moreover, results consolidate the potential of the approach taken by Walters (2013), who adjusted the fracture strain on the basis of the stress triaxiality and mesh size. Specifically, the fracture strain was adjusted on the basis of the L_e/t ratio by providing the lower and upper bound for the fracture data. The lower bound described the fracture initiation in large elements while upper bound described fracture initiation in small elements. For the lower bound the Swift condition was used and for the upper bound a similar fracture envelope to that given by Lou et al. (2012). Despite the fact that size insensitivity in the EBT appears much earlier than predicted by the Swift criterion, current results suggest

this approach could be successfully employed between the UAT and PST.

The investigation of localization in the PST and EBT specimen required a geometric imperfection in the model. Although this defect was small, size of the defect might influence the results. Therefore, the influence of the inhomogeneity on the fracture strain was determined by running two additional simulations. In the PST model, the severity of the defect was increased from $f = 0.99$ to $f = 0.89$ (10%). In the EBT model, the severity of the defect remained the same, but instead of the groove an imperfection was reduced to a single node in a middle of the model. As a result, in the PST the fracture strain increased by approximately ∼3% for both AU6 and 10. In the EBT path, the localization was not predicted and thus, size effects were removed completely.

4.2. Softening

A separate issue that has surfaced in the present study is the softening of the stress–strain curve once the localized necking sets in, especially along the UAT path. This also stresses the importance of considering the equivalent stress as one of the field quantities for which volume averaged response is calculated. Evidently, the softening is related to the equivalent stress drop and unloading of the models outside of the localization zone, as observed in Fig. 5. In the EBT no unloading happens and there is also no softening. We note that the stress drop, and the associated softening, is not limited to the large scale currently in focus, and has previously been shown to appear as a result of void nucleation in several micromechanical studies, e.g. (Fleck et al., 1989; Hutchinson and Tvergaard, 1989; Barsoum and Faleskog, 2011).

5. Summary and conclusions

In this paper, the size effects in multi-axial tension are analyzed numerically. Specifically, three different stress states are

considered: uniaxial tension ($\eta = 1/3$), plane strain tension ($\eta = 1/\sqrt{3}$) and equi-biaxial tension ($\eta = 2/3$). The method employed involves averaging the field quantities over a chosen volume, the size of which is characteristic to large shell elements commonly used in large-scale structural analysis involving fracture initiation. Two averaging volumes were considered: AU6 and AU10, with the element length and thickness ratio L_e/t being 6 and 10, respectively.

Analyses of the macroscopic equivalent stress and plastic strain in the AUs allowed the fracture strain to be determined as a function of stress triaxiality. The results clearly show that the fracture strain sensitivity to the AU size is a strong function of the stress state in the sheet material. In the uniaxial tension the size effects are much stronger than observed in the equi-biaxial and plane strain tension. Consequently, the shape of the fracture envelope that is valid for small-scale analysis changes considerably when a fracture initiation in large shell elements is considered. This explains the success of *shear* criterion in simulations involving large shell elements, e.g. (Naar et al., 2002).

The results of the analyses with the shell elements correspond well to the solid element results in the case of the UAT. In the EBT and PST path the shell elements are unable to resolve the deformations correctly because of the necking in the thickness direction. We emphasize that the current results remain valid for the strain paths analyzed, i.e., the macroscopic time-averaged stress triaxiality remains constant throughout the deformation history. However, the fracture initiation strain also depends strongly on the loading path, (Dunand and Mohr, 2010). Future work must determine the influence of the loading path on the size effects. Furthermore, in applications to thicker plates it must be ensured that macroscopic response in the averaging unit complies with the plane stress condition, otherwise the applicability to large shell elements, $L_e/t > 5$, is questionable. This investigation was limited to membrane action, thus the influence of bending is omitted. In cases of very sturdy plates, the bending might become important. Thus, the approach needs to be validated for these cases as well. This is left for future work. Additionally, different steel grades should be considered.

Acknowledgments

Appendix A

In the EBT model only in-plane (x–y) symmetry could be employed because ABAQUS does not support overlapping boundary conditions in the same region in two different coordinate systems. The displacement at the edge of the specimen was applied in the cylindrical coordinate system, while the symmetry condition had to be applied in the rectangular coordinate system. This is due to the geometric imperfection introduced into the FE model in the y-direction. The severity of the geometric imperfection was adjusted in such a way that the localized equivalent strain would be at least 10% higher than the equivalent strain outside of the neck.

Appendix B

Table B1
True stress plastic strain curve used in numerical simulations.

True stress	Plastic strain
349.00	0.000
356.00	0.036
375.57	0.041
400.61	0.055
418.88	0.069
433.52	0.083
446.10	0.097
457.91	0.111
468.83	0.125
481.82	0.144
493.69	0.165
508.14	0.186
523.19	0.211
537.94	0.241
552.61	0.276
575.66	0.327
599.47	0.387
627.92	0.475
657.15	0.573
675.60	0.639
698.25	0.718
721.11	0.803
734.65	0.863
744.88	0.921
760.84	0.995
765.30	1.027

Appendix C

Forms of fracture and instability criteria used in this study are summarized as follows:

BWH criterion (Alsos et al., 2008), formulated in terms of principal strain ratio $\beta = \varepsilon_2/\varepsilon_1$ and assuming that $\hat{\varepsilon}_1 = n$:

$$\sigma_1 = \begin{cases} \frac{2K}{\sqrt{3}} \frac{1+0.5\beta}{\sqrt{1+\beta+\beta^2}} \left(\frac{2}{\sqrt{3}} \frac{\hat{\varepsilon}_1}{1+\beta} \sqrt{1+\beta+\beta^2} \right)^n & \text{if } \beta \leqslant 0, \\ \frac{2K}{\sqrt{3}} \frac{\left(\frac{2}{\sqrt{3}} \hat{\varepsilon}_1 \right)^n}{\sqrt{1 - \left(\frac{\beta}{2+\beta} \right)^2}}, & \text{otherwise,} \end{cases} \quad (C.1)$$

where $K = 750$ is the strength coefficient and $n = 0.24$ is the strain hardening exponent.

RTCL damage criterion (Törnqvist, 2003):

$$D = \frac{1}{\bar{\varepsilon}_f} \int_0^{\bar{\varepsilon}_f} \begin{cases} 0 & \text{if } \eta < -1/3, \\ \frac{\sigma_1}{\bar{\sigma}} d\bar{\varepsilon}^p & \text{if } -1/3 \leqslant \eta \leqslant 1/3, \\ \exp\left(\frac{3\eta-1}{2}\right) d\bar{\varepsilon}^p & \text{otherwise,} \end{cases} \quad (C.2)$$

where σ_1 is the first principal stress.

Lou criterion (Lou et al., 2012):

$$\left(\frac{2\tau_{max}}{\bar{\sigma}} \right)^{C_1} \left(\frac{\langle 1+3\eta \rangle}{2} \right)^{C_2} \bar{\varepsilon}_f = C_3 \langle \chi \rangle = \begin{cases} \chi \text{ when } \chi \geqslant 0 \\ 0 \text{ when } \chi < 0 \end{cases}, \quad (C.3)$$

where τ_{max} is the maximum shear stress, and calibration parameters for the current fit: $C_1 = 5$, $C_2 = 0$ and $C_3 = 1.05$.

Swift principal instability strains (Swift, 1952), assuming a constant stress ratio $\alpha = \sigma_2/\sigma_1$ are (Broekhuijsen, 2003):

$$\begin{aligned} \varepsilon_1 &= \frac{2(2-\alpha)(1-\alpha+\alpha^2)}{4-3\alpha-3\alpha^2+4\alpha} n, \\ \varepsilon_2 &= \frac{2(2\alpha-1)(1-\alpha+\alpha^2)}{4-3\alpha-3\alpha^2+4\alpha} n. \end{aligned} \quad (C.4)$$

They are converted into the equivalent plastic strain and stress triaxiality space using following equations, (Lee, 2005):

$$\bar{\varepsilon} = \frac{2}{\sqrt{3}} \sqrt{1 + \beta + \beta^2} \cdot \varepsilon_1,$$

$$\eta = \frac{1}{\sqrt{3}} \frac{1 + \beta}{\sqrt{1 + \beta + \beta^2}}, \tag{C.5}$$

where $\beta = \varepsilon_2 / \varepsilon_1$.

References

ABAQUS, 2011. ABAQUS Analysis User's Manual, Version 6.11, Dassault Systèmes Simulia Corporation.

Alsos, H.S., Amdahl, J., Hopperstad, O.S., 2009. On the resistance to penetration of stiffened plates. Part II: Numerical analysis. Int. J. Impact Eng. 36 (7), 875–887.

Alsos, H.S., Hopperstad, O.S., Törnqvist, R., Amdahl, J., 2008. Analytical and numerical analysis of sheet metal instability using a stress based criterion. Int. J. Solids Struct. 45 (7–8), 2042–2055.

Bao, Y., Wierzbicki, T., 2004. On fracture locus in the equivalent strain and stress triaxiality space. Int. J. Mech. Sci. 46 (1), 81–98.

Barsoum, I., Faleskog, J., 2011. Micromechanical analysis on the influence of the Lode parameter on void growth and coalescence. Int. J. Solids Struct. 48 (6), 925–938.

Barsoum, I., Faleskog, J., 2007. Rupture mechanisms in combined tension and shear—Experiments. Int. J. Solids Struct. 44 (6), 1768–1786.

Bazant, Z.P., 2000. Size effect. Int. J. Solids Struct. 37 (1), 69–80.

Beese, A.M. et al., 2010. Partially coupled anisotropic fracture model for aluminum sheets. Eng. Fract. Mech. 77 (7), 1128–1152.

Broekhuijsen, J., 2003. Ductile Failure and Energy Absorption of Y-Shape Test Section (Masters thesis). Delft University of Technology.

Dequiedt, J.L., 2011. Localization in elasto-plastic materials: influence of an evolving yield surface in biaxial loading conditions. Int. J. Solids Struct. 48 (16–17), 2324–2332.

Dunand, M., Mohr, D., 2010. Hybrid experimental–numerical analysis of basic ductile fracture experiments for sheet metals. Int. J. Solids Struct. 47 (9), 1130–1143.

Ehlers, S., 2010. The influence of the material relation on the accuracy of collision simulations. Mar. Struct. 23 (4), 462–474.

Ehlers, S., Varsta, P., 2009. Strain and stress relation for non-linear finite element simulations. Thin Wall. Struct. 47 (11), 1203–1217.

Ehlers, S. et al., 2008. Simulating the collision response of ship side structures: a failure criteria benchmark study. Int. Shipbuild. Prog. 55 (1), 127–144.

Fleck, N.A., Hutchinson, J.W., 1993. A phenomenological theory for strain gradient effects in plasticity. J. Mech. Phys. Solids 41 (12), 1825–1857.

Fleck, N.A., Hutchinson, J.W., Tvergaard, V., 1989. Softening by void nucleation and growth in tension and shear. J. Mech. Phys. Solids 37 (4), 515–540.

Ghahremaninezhad, A., Ravi-Chandar, K., 2012. Ductile failure behavior of polycrystalline Al 6061-T6. Int. J. Fract. 174 (2), 177–202.

Gruben, G., Hopperstad, O.S., Børvik, T., 2012. Simulation of ductile crack propagation in dual-phase steel. Int. J. Fract. 180 (1), 1–22.

Gurson, A.L., 1977. Continuum theory of ductile rupture by void nucleation and growth. Part I – Yield criteria and flow rules for porous ductile media. J. Eng. Mater. Technol. 99 (1), 2–15.

Haltom, S.S., Kyriakides, S., Ravi-Chandar, K., 2013. Ductile failure under combined shear and tension. Int. J. Solids Struct. 50 (10), 1507–1522.

Hancock, J.W., Mackenzie, A.C., 1976. On the mechanisms of ductile failure in high-strength steels subjected to multi-axial stress-states. J. Mech. Phys. Solids 24 (2), 147–160.

Hogström, P., Ringsberg, J.W., 2012. An extensive study of a ship's survivability after collision – a parameter study of material characteristics, non-linear FEA and damage stability analyses. Mar. Struct. 27 (1), 1–28.

Hogström, P., Ringsberg, J.W., 2013. Assessment of the crashworthiness of a selection of innovative ship structures. Ocean Eng. 59 (c), 58–72.

Hogström, P., Ringsberg, J.W., Johnson, E., 2009. An experimental and numerical study of the effects of length scale and strain state on the necking and fracture behaviours in sheet metals. Int. J. Impact Eng. 36 (10–11), 1194–1203.

Hopperstad, O.S. et al., 2003. On the influence of stress triaxiality and strain rate on the behaviour of a structural steel. Part I. Experiments. Eur. J. Mech. A – Solid 22 (1), 1–13.

Hu, J., Marciniak, Z., Duncan, J., 2002. Mechanics of Sheet Metal Forming, second ed. Butterworth–Heinemann.

Hutchinson, J.W., Neale, K.W., 1979. Sheet necking – II. Time-independent behavior. In: Koistinen, D.P., Wang, N.M. (Eds.), Mechanics of Sheet Metal Forming. Springer, pp. 127–153.

Hutchinson, J.W., Tvergaard, V., 1989. Softening due to void nucleation in metals. In: Fracture Mechanics: Perspective and Directions (20th Symposium), ASTM STP (1020), pp. 61–83.

Johnson, G.R., Cook, W.H., 1985. Fracture characteristics of three metals subjected to various strains, strain rates, temperatures and pressures. Eng. Fract. Mech. 21 (1), 31–48.

Kõrgesaar, M., Ehlers, S., 2010. An assessment procedure of the crashworthiness of an LNG tanker side structure. Ship Technol. Res. 50 (2), 108–119.

Lee, Y.-W., 2005. Fracture Prediction in Metal Sheets (Doctoral thesis). Ph.D thesis in the Department of Ocean Engineering in MIT.

Li, Y., Karr, D.G., 2009. Prediction of ductile fracture in tension by bifurcation, localization, and imperfection analyses. Int. J. Plast. 25 (6), 1128–1153.

Lou, Y., Huh, H., Lim, S., Pack, K., 2012. New ductile fracture criterion for prediction of fracture forming limit diagrams of sheet metals. Int. J. Solids Struct. 49 (25), 3605–3615.

Luo, M., Wierzbicki, T., 2010. Numerical failure analysis of a stretch-bending test on dual-phase steel sheets using a phenomenological fracture model. Int. J. Solids Struct. 47 (22–23), 3084–3102.

Marciniak, Z., Kuczyński, K., 1967. Limit strains in the processes of stretch-forming sheet metal. Int. J. Mech. Sci. 9 (9), 609–620.

McClintock, F.A., 1968. A criterion for ductile fracture by the growth of holes. J. Appl. Mech. 35, 363.

Naar, H., Kujala, P., Simonsen, B.C., Ludolphy, H., 2002. Comparison of the crashworthiness of various bottom and side structures. Mar. Struct. 15 (4), 443–460.

Rice, J.R., Tracey, D.M., 1969. On the ductile enlargement of voids in triaxial stress fields. J. Mech. Phys. Solids 17 (3), 201–217.

Samuelides, M., 2012. Designing for protection against collision. In: Guedes Soares, C., Garbatov, Y., Fonseca, N., Texeira, A.P. (Eds.), Marine Technology and Engineering, pp. 955–977.

Simonsen, B.C., Törnqvist, R., 2004. Experimental and numerical modelling of ductile crack propagation in large-scale shell structures. Mar. Struct. 17 (1), 1–27.

Swift, H.W., 1952. Plastic instability under plane stress. J. Mech. Phys. Solids 1 (1), 1–18.

Tardif, N., Kyriakides, S., 2012. Determination of anisotropy and material hardening for aluminum sheet metal. Int. J. Solids Struct. 49 (25), 3496–3506.

Tasan, C.C., Hoefnagels, J.P.M., ten Horn, C.H.L.J., Geers, M.G.D., 2009. Experimental analysis of strain path dependent ductile damage mechanics and forming limits. Mech. Mater. 41 (11), 1264–1276.

Tvergaard, V., 1993. Necking in tensile bars with rectangular cross-section. Comput. Method. Appl. Mech. Eng. 103 (1), 273–290.

Törnqvist, R., 2003. Design of Crashworthy Ship Structures (Doctoral thesis). DTU.

Walters, C.L., 2013. Framework for adjusting for both stress triaxiality and mesh size effect for failure of metals in shell structures. Int. J. Crashworthiness, 1–12.

Xue, L., 2010. Localization conditions and diffused necking for damage plastic solids. Eng. Fract. Mech. 77 (8), 1275–1297.

Yamada, Y., Endo, H., Pedersen, P.T., 2005. Numerical study on the effect of buffer bow structure in ship-to-ship collisions. In: Proceedings of the 15th (2005) International Offshore and Polar Engineering Conference (ISOPE), Seoul, Korea, June 19–24, 2005.

Zhang, Z.L., Hauge, M., Ødegård, J., Thaulow, C., 1999. Determining material true stress-strain curve from tensile specimens with rectangular cross-section. Int. J. Solids Struct. 36 (23), 3497–3516.